

Global Health Effects of Future Atmospheric Mercury Emissions

Yanxu Zhang (✉ zhangyx@nju.edu.cn)

Nanjing University <https://orcid.org/0000-0001-7770-3466>

Zhengcheng Song

Nanjing University

Shaojian Huang

Nanjing University

Peng Zhang

Nanjing University

Yiming Peng

Nanjing University

Peipei Wu

Nanjing University

Jing Gu

Nanjing University

Stephanie Dutkiewicz

Massachusetts Institute of Technology

Huanxin Zhang

Department of Chemical and Biochemical Engineering

Shiliang Wu

Michigan Technological University

Feiyue Wang

University of Manitoba <https://orcid.org/0000-0001-5297-0859>

Long Chen

East China Normal University <https://orcid.org/0000-0001-9574-7307>

Shuxiao Wang

School of Environment, Tsinghua University China <https://orcid.org/0000-0001-9727-1963>

Ping Li

State Key Laboratory of Environmental Geochemistry, Institute of Geochemistry, Chinese Academy of Science

Keywords: Mercury (HG), global health effects, atmospheric emissions

Posted Date: January 12th, 2021

DOI: <https://doi.org/10.21203/rs.3.rs-136067/v1>

License:  This work is licensed under a Creative Commons Attribution 4.0 International License.

[Read Full License](#)

Version of Record: A version of this preprint was published at Nature Communications on May 24th, 2021. See the published version at <https://doi.org/10.1038/s41467-021-23391-7>.

Abstract

Mercury (Hg) is a potent neurotoxin that poses health risks to the global population. Anthropogenic Hg emissions to the atmosphere are projected to decrease in the future due to enhanced policy efforts such as the Minamata Convention, a legally-binding international treaty entered into force in 2017. To project the health benefits of emission reduction requires considering both primary sources and recycling of previously deposited Hg from the land and ocean. Here we report the development of a comprehensive climate-atmosphere-land-ocean-ecosystem and exposure-risk model framework for Hg and its application to project the health effects of future atmospheric emissions. We find the projected Hg health risk changes nonlinearly with emission changes, and the most optimistic scenario (maximum feasible reduction, MFR) leads to Hg levels in the freshwater and marine biota half of the present-day levels. Our results show that the accumulated health effects associated with Hg exposure during 2010–2050 are \$19 (range: 10–27) trillion (2020 USD) realized to 2050 (3% discount rate) for the current policy scenario. The MFR scenario is projected to have a health benefit of \$2.4 trillion, while a business-as-usual scenario results in an additional \$4.9 trillion health loss. Our results suggest a substantial increase in global human health cost if emission reduction actions are delayed. This comprehensive modeling approach provides a much-needed tool to help parties to evaluate the effectiveness of Hg emission controls as required by the Minamata Convention.

Introduction

Mercury (Hg) is a global pollutant that is associated with impaired neurocognitive deficits in human fetuses and cardiovascular effects in adults (Axelrad et al., 2007; Roman et al., 2011). Human exposure to Hg is predominantly via the consumption of food (e.g., seafood and rice) that contain methylmercury (MeHg), the most toxic form of Hg (Bellanger et al., 2013). The annual death from the fatal heart attack that is attributable to MeHg exposure is estimated to be over 10,000 in China and the U.S. (Chen et al., 2019; Giang & Selin, 2016). Economic losses from intelligence quotient (IQ) decrease of developing brains associated with MeHg exposure has been estimated at \$16 billion in the U.S. and European Union (Bellanger et al., 2013; Chen et al., 2019; P. Grandjean et al., 2012). To protect human health and the environment, the Minamata Convention on Mercury, a legally-binding international treaty, took effect in August 2017 to reduce anthropogenic emissions of Hg (UNEP, 2017).

Future projections of global primary anthropogenic Hg emissions vary drastically driven by underlying social-economic and technological change (Pacyna et al., 2016; Streets et al., 2009). The re-emissions from soils and oceans that receive past atmospheric depositions of Hg (legacy emissions) are also important sources, the magnitude of which is 2–3 times larger than the primary anthropogenic emissions (Horowitz et al., 2017; Selin et al., 2008). The MeHg exposure is influenced by a chain of processes including atmospheric emission, atmospheric transport and deposition, air-sea exchange, air-land exchange, chemical transformation (especially Hg methylation), food web transfers, and human food intake (Giang & Selin, 2016). These processes are modulated by the fluctuation and change in climate, land-use, ocean circulation, and ecosystem functions (Schartup et al., 2019; H Zhang et al., 2016). Earlier

studies do not link emissions to exposure changes (Bellanger et al., 2013; Griffiths et al., 2007; Rice et al., 2010; Spadaro & Rabl, 2008; Trasande et al., 2005). Later efforts in global Hg exposure modeling have considered only a subset of these processes. For instance, using atmospheric transport models, atmospheric deposition is considered as an indicator for the level of MeHg in seafood (Chen et al., 2019; Giang & Selin, 2016; H Zhang et al., 2016). Zhang et al. (2016) included the impact of changing climate, land-use, and land-cover on atmospheric transport and deposition, and Amos et al. (2013) and Angot et al. (2018) considered the response of land/ocean re-emissions to anthropogenic emission change with a box model.

In this study, we develop a more comprehensive approach to project the change in human MeHg exposure responding to Hg emission changes. We integrate changes in anthropogenic emissions, climate, and biogeochemical cycles. We use a coupled three-dimensional atmosphere/ocean and two-dimensional land model. The Hg/MeHg levels in the environment are used to scale an intake inventory of MeHg for different countries, which are further used to calculate the health impact based on epidemiology-based dose-response relationships (see Methods for details). We present a map of MeHg-related health risks for all the countries for the first time. Based on this, we translate future Hg emission projections into health risks, and to help parties and stakeholders to evaluate impacts from changes in Hg emissions.

Results And Discussion

Baseline Hg-related health risk. We estimate that the global health impacts associated with MeHg exposure for the general population are \$117 billion (2020 USD adjusted by purchasing power parity, PPP), contributed by 1.2×10^7 points of IQ decrements (0.086 point per-fetus) and 29,000 deaths per year at present-day. We include two health endpoints as a consequence of food MeHg exposure: decrement in IQ of newborns and fatal heart attack (FHA) for general populations. The IQ decrement is transferred to lifelong earn loss based on the projections of the population and economic growth of each country (Bellanger et al., 2013; Rice & Hammitt, 2005). The economic loss from FHA is calculated based on a value of statistical life (VSL) approach, which is scaled by the PPP adjusted per-capita GDP value of individual countries (Giang & Selin, 2016). The exposures from seafood (including fish and aquatic animals), freshwater fish (also including other aquatic animals), and rice consumption are included here with the MeHg concentrations from literature (see Method for more details and the Supporting Information for detailed data).

We find that the population's dietary choices are vital factors influencing MeHg exposure and health risk. Coastal countries with large seafood consumption have the largest MeHg exposure, and rice and freshwater fish consumption are not negligible in some countries (Figure S5). The highest seafood MeHg exposure is found in countries with large seafood consumption, such as the Maldives (33 $\mu\text{g}/\text{d}$), Greenland (16 $\mu\text{g}/\text{d}$), Iceland (15 $\mu\text{g}/\text{d}$), and Kiribati (13 $\mu\text{g}/\text{d}$) (Figure S5). The national average per-capita seafood consumptions are 190, 89, 74, and 48 kg/y for these four countries, respectively, which are much higher than the global average of 15 kg/y (UN FAO, <http://www.fao.org>). The lowest risk is found in

inland countries with nearly no seafood consumption, such as Ethiopia (0.0018 $\mu\text{g}/\text{d}$), Uganda (0.0093 $\mu\text{g}/\text{d}$), and Chad (0.014 $\mu\text{g}/\text{d}$). The MeHg exposure from rice is the highest in Southeast Asian countries such as Indonesia (1.7 $\mu\text{g}/\text{d}$), Laos (0.90 $\mu\text{g}/\text{d}$), and Cambodia (0.77 $\mu\text{g}/\text{d}$) (Figure S5). The contribution of rice to MeHg exposure has previously been found in communities relying on rice grown in areas heavily contaminated with Hg (Rothenberg et al., 2014; Hua Zhang et al., 2010), whereas our findings highlight the potential importance of rice consumption for the general population. We find the contribution from rice could be dominant in inland countries with large rice consumptions, e.g., Nepal (58%), Afghanistan (50%), and Bhutan (45%). The spatial distribution of the consumption of freshwater fish is similar to that of rice, and the exposure is the highest in Asian countries such as Cambodia (6.3 $\mu\text{g}/\text{d}$), Myanmar (3.5 $\mu\text{g}/\text{d}$), and Japan (2.9 $\mu\text{g}/\text{d}$). The MeHg exposure from this pathway is also influenced by the fish MeHg concentrations, which causes relatively high exposure over countries such as Russia (3.5 $\mu\text{g}/\text{d}$) and Finland (3.2 $\mu\text{g}/\text{d}$).

The total health risk of MeHg reflects the total exposure of the above-discussed pathways. The associated IQ decrease per-fetus is the highest in the Maldives (1.2 points), Greenland (0.60 points), and Iceland (0.56 points), where the exposure from seafood is high. The risk is the lowest in Uzbekistan (0.0040 points), Tajikistan (0.0036 points), and Ethiopia (0.0012 points), where the consumption of fish and rice are both low (Fig. 1A). Figure 1C shows the economic loss due to IQ reduction of newborns. Besides MeHg exposure, the loss reflects the birth rate and income level of countries. The US ranks first by losing \$12 billion per year, followed by China (\$7.3 billion), Japan (\$6.2 billion), and Russia (\$2.9 billion). The spatial pattern of the deaths associated with FHA (Fig. 1B) is quite different from that of IQ decrement but reflects the total population and baseline FHA incidence. The most deaths are from populous countries with mild to high per-capita risks, such as China (5,600 per year), Russia (3,200), Indonesia (3,200), and India (2,300). Taking into the difference in VSL per death puts Russia the first place (\$9.1 billion) in economic loss from this pathway, followed by the USA (\$9.0 billion), China (\$7.7 billion), and Japan (\$3.2 billion) (Fig. 1D). Combining the two endpoints results in that the US suffers from a total loss of \$21 billion per year, followed by China (\$15 billion), Russia (\$12 billion), and Japan (\$9.3 billion) (Fig. 1E). Asia (\$48 billion), Europe (\$34 billion), and North America (\$23 billion) have 90% of the global health risk, with Africa (\$6.4 billion), South America (\$5.4 billion), and Oceania (\$1.5 billion) contributing the remaining 10%.

Our study, to our knowledge, is the first effort to estimate the health risk associated with MeHg exposure based on food intake inventory and food MeHg concentrations for individual countries at a global scale. Validation data remain sparse but our estimate generally agrees with previous regional-scale studies for China, US and Europe. Our results for the Chinese population (0.11 point IQ decrease per fetus and 5600 FHA deaths per year) are slightly lower than Chen et al. (2019) (0.14 points per fetus and 7360 deaths), as we exclude the exposure from other food such as pork, beef, and eggs, which have limited MeHg concentration data. We estimate the MeHg exposure from seafood consumption for the US population is $11 \mu\text{g kg body wt}^{-1} \text{ a}^{-1}$, which agrees with the estimate of Mahaffey et al. (2004) and Sunderland (2007): $7.3\text{--}11 \mu\text{g kg}^{-1} \text{ a}^{-1}$. We estimate a total of 500,000 points per year of IQ decrements in the US,

which is higher than previous estimates (264,000-285,000 points per year) (Bellinger, 2012; P. Grandjean et al., 2012), but our estimate (720,000 points) for Europe agrees well with Bellinger et al. (2013), who calculated 640,000 points of IQ loss based on hair Hg concentrations among women of reproductive age.

The modeled spatial pattern agrees with the distribution of Hg biomarkers in general populations from individual countries (Figure S4). We estimate the hair and blood Hg concentrations based on the total food MeHg exposure and pharmacokinetics models (see Method for details), and evaluate them against available human biomarker data in literature as summarized by Basu et al. (2018). The estimated blood Hg concentrations among the 40 countries where data are available are $2.5 \pm 1.8 \mu\text{g/L}$ (mean \pm standard deviation), consistent with measured values ($2.2 \pm 2.1 \mu\text{g/L}$) with a correlation coefficient of 0.71 (Figure S4). The measured highest mean blood Hg concentrations are found in Greenland ($9.2 \mu\text{g/L}$), which is well captured by our estimate ($10 \mu\text{g/L}$, rank = 1st). High blood Hg concentrations are also measured in Cambodia ($9.1 \mu\text{g/L}$), Spain ($6.0 \mu\text{g/L}$), Japan ($5.1 \mu\text{g/L}$), and South Korea ($4.0 \mu\text{g/L}$), and our estimates agree with these measurements ($4.8, 3.4, 5.5,$ and $4.6 \mu\text{g/L}$, respectively). A lower correlation coefficient (0.53) is calculated for the estimated and measured hair Hg concentrations ($n = 38$), but the estimate ($0.40 \pm 0.27 \mu\text{g/g}$) is within a factor of ~ 2 from the measured data ($0.76 \pm 0.48 \mu\text{g/g}$) (Figure S4). It is not surprising that our results agree better with blood Hg than hair Hg, as the former reflects a shorter-term exposure while the latter subjects to more intrinsic (such as genetics) factors (Basu et al., 2018; Eagles-Smith et al., 2018). Overall, our results show that human Hg biomarker levels could be explained by the food Hg exposure for general populations from individual countries, supporting our approach can be used to assess the baseline risk at present-day and its projection in the future.

Future Hg emissions. Figure 2 shows global anthropogenic Hg emissions projections under different scenarios. The global total anthropogenic Hg emissions are 1890 Mg yr^{-1} in 2010 with artisanal and small-scale gold mining (ASGM, 37%) and fossil fuel combustion (25%) as the two largest sources followed by non-ferrous metals production (10%) and cement production (9%) (AMAP/UNEP, 2013). Streets et al. (2009) projected Hg emissions to increase to 4900 and 3900 Mg yr^{-1} in 2050 under the A1B (business as usual) and A2 (a divided world) scenarios, respectively, driven by the increase of coal combustion in developing countries. In a New Policies (NP) scenario, Pacyna et al. (2016) projected the emissions to decrease to 1020 Mg y^{-1} in 2035. Part of the emission reduction is from fossil fuel combustion and cement production resulting from the co-benefits of greenhouse gas emission control. The Hg emissions from Hg-containing products are also projected to reduce by 70% in 2035 compared to the 2010 situation, and the use of Hg in ASGM is reduced by 46% (Pacyna et al., 2016). In a Maximum Feasible Reduction (MFR) scenario, the global emissions are projected to reduce to 300 Mg y^{-1} with the Hg-containing product and ASGM emissions reduced by 95% and 76%, respectively (Pacyna et al., 2016). The best available technologies are assumed for the industrial and energy sectors without constraints in the economy and increasing demand. Although it was considered an unrealistic scenario for 2035 (Pacyna et al., 2016), we treat it as an optimistic projection for 2050. We refer to this trajectory as the MFR scenario. We also delay the NP scenario from 2035 to 2050 to represent a slower emission reduction pathway (referred to as the NP-Delayed scenario). As a reference, a close to constant emission scenario

(except a slight increase of emissions to 1960 Mg yr^{-1} in 2035) is considered following the Current Policy (CP) scenario of Pacyna et al. (2016). This assumes that the increase in emission activity is balanced by the decrease of emission factors due to continuous emission control (Pacyna et al., 2016).

Future MeHg exposure. We use environmental Hg levels to scale the food Hg concentrations consumed by the general population in the future under various emission change scenarios. The MeHg concentrations in freshwater water fish are influenced by those in their prey and ultimately by river/lake water MeHg levels, which are not explicitly simulated by our integrated model. Instead, we use the atmospheric deposition as a proxy as it is the major source of Hg in surface waters (Rothenberg & Feng, 2012). The rice MeHg concentrations are scaled by soil Hg concentrations due to the strong correlation between them (Kwon et al., 2018). We use the planktonic MeHg concentrations as a proxy for seafood because the uptake from seawater by plankton represents the largest concentration increase for MeHg biomagnification in marine food webs (Schartup et al., 2018).

We find that atmospheric Hg deposition and marine planktonic MeHg are highly sensitive to future Hg emissions (Fig. 3). The atmosphere, ocean, and their exchange are simulated by the GEOS-Chem and MITgcm models, both driven by the meteorological/ocean physical data from climate models. The marine plankton biomass and community structure are modeled by an ecosystem model (see Methods for more details and a model evaluation against observations is in Figure S1-3). The model simulates higher deposition over source regions (e.g., East Asia, West Europe, and North America), regions covered with forests that have larger dry deposition velocity (e.g., South America), and over ocean regions with high precipitations (Fig. 3A). Higher planktonic MeHg concentrations are modeled over productive regions (e.g., high-latitudes and the eastern tropical oceans) (Fig. 3C). The model projects that the MFR and NP-Delayed scenarios reduce the atmospheric deposition in 2050 by 48% and 28%, respectively, compared to the CP scenario. Overall, the decrease of Hg deposition is smaller than that of anthropogenic emissions (85% and 48%, respectively, Fig. 2) because primary emissions only account for 20–30% of total atmospheric Hg emissions (Horowitz et al., 2017). Similarly, the A1B and the A2 scenarios project an increase of primary atmospheric emissions by 150% and 99%, respectively, which only translate to an increase of deposition by 87% and 59%, respectively. The percentage change of planktonic MeHg concentrations is similar to atmospheric deposition, since inorganic Hg, which is the substrate of MeHg in the seawater, is mainly from atmospheric deposition (Y. Zhang et al., 2020). The percentage changes for different regions are predicted to be fairly uniform. Contrasting to atmospheric deposition, the changes in soil Hg concentrations are much smaller, ranging from –3–4% for different scenarios in 2050. This is because of the large mass and long lifetime of Hg in this reservoir (Schuster et al., 2018; Smith-Downey et al., 2010).

Health Effects. The CP scenario projects a flat trend for the global total IQ decrease until 2050 (an increase from 11.1 to 11.6×10^6 pts during 2010–2050) (Fig. 4A), reflecting similar trends in both total MeHg exposure (Fig. 3) and new birth number (World Population Prospects: <https://population.un.org>). We find the changes in future primary anthropogenic emissions are substantially dampened for their health effects. The total IQ decrease in 2050 predicted by the MFR and NP-Delayed scenarios are 24%

and 15% lower than that of the CP scenario, respectively, even though the anthropogenic emissions have been projected to decrease by 85% and 48%, respectively. The A1B and A2 scenarios predict a 51% and 34% increase in the IQ effect, respectively, whereas the changes in primary emissions are 150% and 99%, respectively.

The global population is projected to increase by ~ 40% to 9.7 billion in 2050 (World Population Prospects: <https://population.un.org>), which translates to the projected FHA deaths associated with MeHg exposure by 43% to 40,000 per year for the CP scenario. This results in a cumulative death of 1.6 million during 2010–2050. The increase in total population also cancels the decreasing trend in per-capita exposure of the MFR and NP-Delayed scenarios. The projected trajectory for the deaths of these two scenarios is quite flat, with a cumulative death of 1.4 and 1.5 million, respectively (Fig. 4B). In contrast, the projected deaths for A1B and A2 scenarios are 120% and 94% higher than the level in 2010, amounting to a cumulative death of 2.0 and 1.9 million, respectively.

The economic valuation of these two health endpoints relies on the projection of the global economy, which we adopt the middle-of-the-road pathway projected by the Shared Socioeconomic Pathways (SSP2) in the 21st century (<https://tntcat.iiasa.ac.at/SspDb>). Due to the increase in per-capita GDP, the total economic loss of the CP scenario is projected to increase by a factor of 2.3, and the loss for the strictest emission reduction scenario, MFR, also increases by a factor of 1.4 (Fig. 4C). The cumulative economic loss for the CP scenario is \$19 trillion (2020 USD, discounted to 2050 at a rate of 3%). The projected health benefits of the MFR and NP-Delayed scenarios compared to the CP scenario are \$2.4 trillion and \$1.5 trillion, respectively. On the other hand, the A1B and A2 scenarios will result in an additional loss of \$4.9 trillion and \$3.3 trillion, respectively. The two health endpoints contribute roughly equally to the total loss; however, the contribution from the VSL of FHA becomes more dominant (60%) in 2050 due to a faster increase in total population than new birth.

Uncertainty. We assess the uncertainty and variability of the health effects projected by our integrated model by identifying key driving factors, including food consumption data, food MeHg concentrations, dose-response parameters linking MeHg exposure and health effects, and economic valuation (Fig. 5). We rely on the database of the United Nations' Food and Agriculture Organization (FAO, <http://www.fao.org>) for food consumption. Compared with national data, the two data sources generally agree within a factor of 2 (Figure S6). This reflects both the different survey methods and variability among the population (Cook et al., 2000; A. C. Grandjean, 2012). This results in a variability of cumulative economic loss for the CP scenario as \$10 to \$27 trillion (2020 value and realized in 2050). This variability also propagates to the estimated benefits (or extra costs) for other scenarios (Fig. 5). By considering the log-normal distributions of food MeHg data, the cumulative effects for the CP scenario would range from \$11 to 32 trillion. This indicates that the food intake and MeHg data contribute roughly equally to the uncertainty of exposure calculation. We find that the dose-response functions between MeHg intake and health effects have the largest contribution to the uncertainty, ranging from nearly \$0 to \$48 trillion. This reflects the large variability in the coefficients for IQ decrement and heart attack risk per unit hair Hg increase (Axelrad et al., 2007; Rice et al., 2010; Salonen et al., 1995), despite convincing evidence for the

association between MeHg exposure and human health impact (Karagas et al., 2012). The pharmacokinetics parameters to link food exposure to blood and hair Hg levels play a much smaller role with a variability of 10–20%. Another source of uncertainty comes from the parameters for economic valuation, especially the VSL of heart attack deaths (a factor of 10) (Giang & Selin, 2016). Using high and low assumptions for the economic valuation leads to a range of \$5.0–25 trillion for the health effect of the CP scenario.

Our ability to model the MeHg exposure and risk is limited by existing scientific knowledge and data, such as the food web dynamics of MeHg in higher trophic levels and the dose-response relationships between MeHg exposure and its health effects (Fig. 5). The future Hg emissions to water and soil are subjected to change (Kocman et al., 2017). We only consider the general populations, but not the so called “high exposure” population groups (Basu et al., 2018). The fishery harvest and human food consumption patterns will also change in the future (Cheung, 2018). Our results do not show strong interannual variability for environmental Hg levels on a global scale, but the change in dietary structure and food web dynamics in high trophic levels that are not covered in this model may amplify these variabilities, especially at regional scales (Wang et al., 2019). The permafrost stores a large amount of Hg and may serve as a potential Hg source as a consequence of thawing (Schuster et al., 2018). There are likely other health endpoints not considered in this study due to the limited epidemiological data (Karagas et al., 2012). Our assessment is thus considered illustrative and not a comprehensive projection of impacts. However, much uncertainty of the model framework could be reduced using a similar methodology as science and data evolve.

Policy implications. This study develops and applies a comprehensive climate-atmosphere-land-ocean-ecosystem and exposure-risk model framework for global toxic pollution from Hg. We show that the annual global health risk associated with MeHg exposure is \$117 billion (2020 value), contributed by 1.2×10^7 points of IQ loss and 29,000 heart attack deaths. By 2050, the cumulative health effects are projected to be \$19 (10–27 as uncertainty range) trillion (discount rate of 3% to 2050). Compared to the CP scenario, the MFR and NP-Delayed scenarios have benefits of \$2.4 and \$1.5 trillion, respectively, while the A1B and A2 scenarios have additional losses of \$4.9 and \$3.3 trillion, respectively.

Food availability and population dietary choice are important factors for MeHg exposure and risk. Globally, seafood consumption contributes 56% to the total MeHg exposure, with freshwater fish and rice contributing 34% and 10%, respectively. Coastal and island countries with access to more seafood have the largest seafood consumption and are also the ones with the highest MeHg exposure and health risk. Freshwater fish consumption is the highest in Asian countries, where fish is often raised in rice paddies (Halwart & Gupta, 2004). The rice consumption in these countries is also high. Another important influencing factor is the trophic level of fish/aquatic animals. The mean Hg levels vary for ~ 10 times between the lowest and highest trophic levels, much larger than the impact of water types and whether wild-caught or farm-raised (Figure S7). Dietary guidance on fish selection and consumption frequency is still the rule of thumb for MeHg exposure reduction (Xue et al., 2015). Exceptions are for countries with the least MeHg exposure as found in this study, such as Ethiopia, Tajikistan, and Afghanistan, which are

listed as the countries with serious levels of hunger (Global Hunger Index: <https://www.globalhungerindex.org>). In these countries, the MeHg exposure risk of fish consumption is surpassed by its nutrient benefits (Mozaffarian & Rimm, 2006). We suggest that the Hg level in rice is the most recalcitrant to emission reduction among the three major food categories, and the global contribution from rice consumption could increase to 23% in 2050 under the MFR scenario, which makes limiting rice consumption may be a more important Hg exposure mitigation strategy then.

This study focuses on the MeHg exposure of the general population. Significantly higher exposure and biomarker levels are found for populations exposed to Hg from point sources (e.g., ASGM workers) and populations with high seafood consumption (e.g., Arctic populations that consumes a lot of marine mammals, tropical riverine communities, and coastal and/or small-island communities) (Basu et al., 2018). Although we do not include these two groups due to the lack of global-scale data, to include them will supplement our estimate of MeHg exposure and health risk. With the future improvement of spatial resolution in exposure and risk modeling, our model could also be a useful tool to identify populations that are vulnerable to Hg exposure (Undeman et al., 2018).

We show that the cumulative health effects realized within the 2050 time horizon are not responding linearly with emission changes. The MFR scenario with a rather low emission level in 2050 (300 Mg yr^{-1}) is only 13% lower than the CP scenario. This is associated with the relatively small change in emissions between the two scenarios in the early years (e.g., during 2010–2025), which contributes a large portion to the cumulative health effect realized in 2050 due to its compound interest. Delaying the MFR scenario (i.e., the NP-Delayed scenario) would further reduce the benefit by 38%, not to mention the substantially increased health effects projected for the A1B and A2 scenarios. Even though these estimates are very sensitive to choices of the temporal scope of analysis and evaluation parameters (e.g., VSL, discounting rate) (Giang & Selin, 2016), our results demonstrate the necessity of emission reduction sooner.

The inclusion of land and ocean in our model enables us to directly model the contribution of legacy sources (re-emissions from soil and ocean) without using a scale function (e.g. Selin, 2018) or box models (e.g. Angot et al., 2018). The inclusion of the ocean model coupled with the plankton ecosystem in our integrated model is of great interest because seafood consumption is the major exposure pathway in most countries (Figure S5). The marine plankton and soil Hg concentrations are better proxy data to scale the future change of seafood and rice Hg levels, respectively, than atmospheric deposition that is often employed in previous studies (e.g. Chen et al., 2019; Giang & Selin, 2016).

Our model framework provides a much-needed tool for parties to evaluate the effectiveness of the implementation of the Minamata Convention, especially to assess the response of environmental Hg levels to emission reduction and its implications to human exposure and health risk. Detailed scenario studies using our model framework could be conducted to evaluate and prioritize the health benefits of individual policy measures. For example, as the largest emission source, the control of ASGM is left decided for individual parties and the future emissions have large uncertainty. Our model framework would assist related countries to make their national action plans.

Methods

Mercury transport model. We develop a model framework to simulate the fate and transport of Hg in the Earth system that includes climate, atmosphere, land, ocean, and marine ecosystem (Figure 6). Three-dimensional atmospheric (GEOS-Chem) and oceanic (MITgcm) transport models for Hg are coupled online with a two-dimensional terrestrial mercury model (GTMM). These models are driven by predicted meteorological and ocean circulation data from climate models (GISS GCM ModelE2 and IGSM, respectively). Biogeochemical parameters important for Hg transformation are taken from a marine plankton ecosystem model (Darwin), which is also driven by the IGSM model. The details of these models are elaborated below.

We use the output of the Integrated Global System Modeling (IGSM) framework for the future climate simulated by Sokolov et al. (2009) and Dutkiewicz et al. (2013). Briefly, the model framework includes a three-dimensional ocean model that has a horizontal resolution of $2^\circ \times 2.5^\circ$ and 22 vertical levels from 10 m in the surface to 500 m at depth, and a two-dimensional (latitude and height) atmosphere physical and chemical model. The framework has a terrestrial component with hydrology, vegetation, and natural emissions. The model is run with a pre-industrial level of greenhouse gas concentration for 2000 years as spin up and then for 1860-2000 with observed GHG levels. For the 21st century, a 'business as usual' scenario (close to IPCC AR5 RCP8.5 scenario) is assumed for anthropogenic emissions. We use the IGSM archived monthly mean ocean physics data such as seawater temperature, ocean current velocities, and mixing conditions to drive the MITgcm model (Dutkiewicz et al., 2013).

As the IGSM only contains a two-dimensional atmosphere module, we use the archived future climate data simulated by the NASA Goddard Institute for Space Studies (GISS) general circulation model (GCM) (ModelE2) to drive the GEOS-Chem model (Rind et al., 2007). The model has a horizontal resolution of $2^\circ \times 2.5^\circ$ for the atmosphere, land surface, ocean, and sea ice models. The three-dimensional atmosphere model has 40 vertical levels from the surface to 0.002 hPa (~85 km altitude). The greenhouse gas concentrations are specified following the IPCC AR5 RCP8.5 scenario. The meteorology fields such as temperature and precipitation are archived with a frequency of 3-6 hours. The discrepancies between these two climate models are minimal due to the similar pathways of greenhouse gas concentrations in the 21st century.

The ocean biogeochemistry and ecosystem data are from the Darwin model within the MITgcm framework simulated by Dutkiewicz et al. during the 21st century (2013). This model is driven by the archived ocean physics fields from the IGSM. The transport of inorganic and organic forms of carbon, nitrogen, phosphorus, iron, and silica are included. The model includes six phytoplankton functional groups and two zooplankton grazers (namely diatoms, other large phytoplankton, diazotroph, coccolithophore, *Prochlorococcus*, *Synechococcus*, and small and large herbivorous plankton). The model simulates biogeochemical processes including phytoplankton growth, zooplankton grazing, zooplankton mortality, and the formation and transformation of particulate and dissolved organic

matters. The monthly mean concentrations of organic carbon and plankton biomass, and the rates of plankton growth, grazing, and mortality are archived to drive the Hg component of the model.

We simulate the chemistry, transport, and trophic transfer of Hg in the ocean using the MITgcm following Y. Zhang et al. (2020). The model is driven by ocean physics data from the IGSM and biogeochemical parameters from the Darwin model. The model has the same grid as the ocean component of the IGSM. The model simulates 14 tracers that include elemental Hg, oxidized Hg, monomethylmercury (MMHg), dimethylmercury (DMHg), particulate-bound inorganic Hg, and particulate-bound MMHg, and MMHg in plankton (six phytoplankton groups and two zooplankton types). The model includes a detailed photo- and biological mediated redox chemistry of inorganic Hg, and the transformation with methylated Hg species. The bioaccumulation and biomagnification of MMHg in the marine plankton food web is simulated following Y. Zhang et al. (2020).

The atmospheric chemistry and transport of Hg are simulated by the GEOS-Chem model following Horowitz et al. (2017). The model is based on version v9-02 (www.geos-chem.org). The model has the same resolution as the GISS GCM ModelE2 model and is driven by its archived meteorology fields. The simulated chemistry includes three forms of Hg in the atmosphere: gaseous elemental, gaseous oxidized, and particle-bound Hg. The redox chemistry of Hg is modeled following Horowitz et al. (2017). The chemistry includes two-stage oxidation of elemental Hg by bromine atoms and photoreduction of oxidized Hg in cloud droplets. Concentrations of related chemical species are taken from GEOS-Chem simulation of tropospheric oxidant-aerosol chemistry (Schmidt et al., 2016). The model also includes geogenic and biomass burning sources, as well as reemissions from snow reservoirs (Horowitz et al., 2017).

The soil pool and land-atmosphere exchange of Hg are simulated using the GTMM model (Smith-Downey et al., 2010). The model has a horizontal resolution of $1^\circ \times 1^\circ$ and covers the top 30 cm of soils. The model takes the atmospheric deposition of both elemental and oxidized Hg from GEOS-Chem as input. This part of Hg is assumed to be loosely adsorbed to soil and leaf surfaces and undergoes photoreduction and revolatilization. Part of the Hg can reach to soil pool through litterfall. The model considers four soil Hg pools that are tied to carbon pools with characteristic turnover time ranged from 10^0 to 10^4 years. Hg bound to different soil carbon pools can be transformed between each other, and Hg is released to the atmosphere when the soil carbon is respired by microbial activities. The model is run for 30,000 years with atmospheric deposition at pre-industrial levels before ramped up with monthly deposition from 1840 to 2000 (Smith-Downey et al., 2010).

The GEOS-Chem, GTMM, and MITgcm Hg models are online two-way coupled using a coupler (NJUCPL) following Y. Zhang et al. (2019). With a frequency of 60 mins, atmospheric Hg concentration and deposition data are passed from GEOS-Chem to GTMM and MITgcm, and soil re-emission and ocean evasion fluxes are passed from GTMM and MITgcm to GEOS-Chem, respectively. The initial conditions of these models are taken from previous simulations for the present-day (Horowitz et al., 2017; Smith-Downey et al., 2010; Y. Zhang et al., 2020).

The total anthropogenic Hg emissions for the future are taken from Streets et al. (2009) and Pacyna et al. (2016). Five policy scenarios are developed for the emissions during 2010-2050 (Figure 2). These global total emissions are spatially distributed to each model grid based on the WHET emission inventory for 2010 (Y. Zhang et al., 2016). The spatial distribution and speciation of Hg emissions are assumed to keep constant during the model period. The model is run from 2010 to 2050 for each emission scenario.

Mercury exposure modeling. Figure 7 summarizes the approach we use to estimate MeHg exposure and risk. The MeHg exposure via three food categories is considered in this study: seafood, freshwater fish (including aquatic animals), and rice. Other types of food are ignored because of less data and much lower MeHg concentrations. The per-capita consumption of different food categories for each country is taken from the database of the Food and Agriculture Organization of the United Nations (UN FAO, <http://www.fao.org>).

A database for the average MeHg concentrations of these food categories is developed by collecting available data from the literature (a full list of literature is provided in the Supporting Information). There is a total of 210,000 data points (208,000 for fish/aquatic animals and 6,400 for rice) collected from 395 publications. We exclude the data points near point sources or contaminated sites. The fish/aquatic animals are further divided into two categories: farm-raised and wild-caught with fractions from the UN FAO database. Due to the large concentration variability, we group the fish/aquatic animals into four trophic level bins: 2-2.5, 2.5-3.5, 3.5-4.5, and 4.5-5, and the geometric mean of MeHg concentrations for each trophic level bin is calculated. The trophic level of each fish with reported MeHg concentration and consumption data is from the Fishbase Database (<https://www.fishbase.org>). The fraction of fish consumption for each trophic level bin is estimated based on the marine trophic index if detailed consumption inventory is missing (<http://www.seararoundus.org/mti-fib-rmti/>). We use the global geometric mean concentrations for countries without data. The total MeHg exposure (E) for the general population from each country is calculated as:

$$E = \sum_{i=1}^4 I_{i,j}^{FW\ fish} C_{i,j}^{FW\ fish} + \sum_{i=1}^4 I_{i,j}^{seafood} C_{i,j}^{seafood} + I_{rice} C_{rice}$$

where I and C are for food intake and MeHg concentrations, respectively, for each category [freshwater (FW) fish, seafood, and rice] and trophic level bin i (2-2.5, 2.5-3.5, 3.5-4.5, and 4.5-5) (Figure 7).

Future Mercury exposure. We scale the future population exposure of MeHg based on the exposure level at present-day and the model projected environmental Hg levels (Figure 7). Due to the lack of data, the food consumption pattern is held constant during 2010-2050. The freshwater fish and rice MeHg concentrations for individual countries in a given year are assumed to be proportional to the average total Hg atmospheric deposition (D) (Chen et al., 2019; Giang & Selin, 2016) and total soil Hg concentration (S) (Kwon et al., 2018) in the corresponding country, respectively. For the seafood, we assume the MeHg

exposure of each country for a given year is proportional to the global average plankton MeHg concentrations weighted by the spatial distribution of fish harvest (P) (Watson, 2017):

$$C_{year}^{FW\ fish} = C_{2010}^{FW\ fish} \frac{D_{year}}{D_{2010}}$$

$$C_{year}^{rice} = C_{2010}^{rice} \frac{S_{year}}{S_{2010}}$$

$$C_{year}^{seafood} = C_{2010}^{seafood} \frac{P_{year}}{P_{2010}}$$

Figure 7. Diagram for the approach and data sources for MeHg exposure and risk calculation in this study. Blue frames represent model calculated variables, while black ones are for literature data.

Human health impact. We include two health endpoints in benefit estimates: decrement in IQ of newborns and fatal heart attack (FHA) (Chen et al., 2019; Giang & Selin, 2016; Rice et al., 2010). A linear dose-response relationship without thresholds is recommended by the National Research Council (NRC) between MeHg intake and fetal IQ decrements (Axelrad et al., 2007):

$$\Delta IQ = \gamma \lambda \beta \times \Delta EDI \times BW$$

where ΔIQ is the changes in IQ (points), ΔEDI is the changes in estimated daily intake (EDI) of MeHg, and BW is the average body weight for female adults. The coefficients β ($0.6 \mu\text{g L}^{-1}$ per $\mu\text{g day}^{-1}$), λ ($0.2 \mu\text{g g}^{-1}$ per $\mu\text{g L}^{-1}$), and γ (0.3 IQ points per $\mu\text{g g}^{-1}$) converse from MeHg intake to blood concentration, blood concentrations to hair concentrations, and hair concentrations to IQ decrements, respectively. The total IQ decrements are calculated by multiplying per-fetus IQ decrements and the number of newborns, which are taken from the World Population Prospects by the UN database (<https://population.un.org>). This database includes projections of the total population of both sexes and newborns for each country to 2100.

A log-linear dose-response relationship between MeHg intake and Hg-related fatal heart attacks is used in this study (Chen et al., 2019):

$$\Delta CF = \sum_g POP_g \times Cf_g \times \omega \times (1 - e^{-\varphi \lambda \beta \times \Delta EDI \times BW})$$

where ΔCF is the changes in the deaths from fatal heart attacks associated with MeHg exposure, POP_g is the population of gender g (male and female) from World Population Prospects, and Cf_g is the age-adjusted incidence of FHA of gender g from Global Health Estimates by World Health Organization (http://www.who.int/healthinfo/global_burden_disease). The coefficient φ (0.066 per $\mu\text{g g}^{-1}$) converses

hair MeHg concentrations to fatal heart attack risks. The subjective coefficient ω (0.33) represents the probability of the causality of the associations, reflecting the substantial uncertainties due to limited epidemiological studies.

For model evaluation, we also calculated the averaged Hg concentrations in the blood (C^{blood}) and the hair (C^{hair}):

$$C^{blood} = \beta \times EDI \times BW$$

$$C^{hair} = \lambda \times C^{blood}$$

The modeled Hg biomarker concentrations for individual countries are compared with the geometric mean of measured data (961,000 data points) from 245 publications for 83 countries and regions (a full list of literature is provided in the Supporting Information). The blood and hair Hg concentrations for general population are used by excluding high exposure group data (high fish consumption population or population exposed to point Hg sources such as ASGM and Hg mines).

Economic valuation. The IQ decrements are converted to monetary values using \$18,832 (2008 value) per IQ point normalized by the ratio between the PPP-adjusted GDP per capita in each country and the US (Bellanger et al., 2013). The economic loss from FHA deaths associated with MeHg exposure is calculated by a value of statistical life (VSL) approach. We adopt a VSL per death of \$6.3 million (2005 value) following Giang and Selin (2016). This value is also normalized by the PPP-adjusted GDP per capita in each country. The sum of these two endpoints is calculated as the total economic loss. The economic data is taken from the shared socioeconomic pathways database that projects the GDP growth for each country in the 21st century (<https://tntcat.iiasa.ac.at/SspDb>). We use the SSP2 scenario that assumes a median level of GDP growth rate. A discount rate of 3% is used to realize the economic loss from 2010-2050 to 2050 (Giang & Selin, 2016).

Uncertainty analysis. We consider the contribution of the data and parameters for food consumption, food MeHg concentrations, dose-effect relationship, and economic valuation to the total uncertainty. We compare the food consumption data from UN FAO with national datasets (details available in the Supporting Information). The difference between them is used to represent the uncertainty range of the FAO datasets. For food MeHg concentration, we use the standard deviation of the log-transformed concentrations in each food category to represent its uncertainty ($\mu+\sigma$ and $\mu-\sigma$ as high- and low-end values, respectively). We use the ranges (or standard deviations) of the dose-effect relationship between MeHg exposure and its health effect summarized by Chen et al. (2019). For per-IQ earn loss, we use a high- and low-end value of \$18832 and \$8013, respectively (Giang & Selin, 2016). The VSL per death ranges from \$1 to \$10 million following Giang & Selin (2016).

Declarations

Acknowledgments

We thank Aijun Ding, Bin Wang, Guoxing Li, Qingru Wu, Lars-Eric Heimbürger, Noelle Selin, and Elsie Sunderland for helpful discussions. The authors gratefully acknowledge financial support from the National Natural Science Foundation of China (NNSFC) 41875148, Start-up fund from the Thousand Youth Talents Plan, Jiangsu Innovative and Entrepreneurial Talents Plan, the Collaborative Innovation Center of Climate Change, Jiangsu Province.

Data availability

All data and model algorithms are available in the Extended Data and Supplementary Information.

Code availability

All model code is available at the following link: http://ebmg.online/model_hg.html.

References

- AMAP/UNEP. (2013). Technical Background Report for the Global Mercury Assessment. *Arctic Monitoring and Assessment Programme*, 263. Retrieved from <http://www.amap.no/documents/doc/technical-background-report-for-the-global-mercury-assessment-2013/848>
- Amos, H. M., Jacob, D. J., Streets, D. G., & Sunderland, E. M. (2013). Legacy impacts of all-time anthropogenic emissions on the global mercury cycle. *Global Biogeochemical Cycles*, 27(2), 410–421. <https://doi.org/10.1002/gbc.20040>
- Angot, H., Hoffman, N., Giang, A., Thackray, C. P., Hendricks, A. N., Urban, N. R., & Selin, N. E. (2018). Global and Local Impacts of Delayed Mercury Mitigation Efforts. <https://doi.org/10.1021/acs.est.8b04542>
- Axelrad, D. A., Bellinger, D. C., Ryan, L. M., & Woodruff, T. J. (2007). Dose-response relationship of prenatal mercury exposure and IQ: An integrative analysis of epidemiologic data. *Environmental Health Perspectives*, 115(4), 609–615. <https://doi.org/10.1289/ehp.9303>
- Basu, N., Horvat, M., Evers, D. C., Zastenskaya, I., Weihe, P., & Tempowski, J. (2018). A state-of-the-science review of mercury biomarkers in human populations worldwide between 2000 and 2018. *Environmental Health Perspectives*, 126(10), 1–14. <https://doi.org/10.1289/EHP3904>
- Bellanger, M., Pichery, C., Aerts, D., Berglund, M., Castaño, A., Čejchanová, M., et al. (2013). Economic benefits of methylmercury exposure control in Europe: Monetary value of neurotoxicity prevention. *Environmental Health: A Global Access Science Source*, 12(1), 1–10. <https://doi.org/10.1186/1476-069X-12-3>
- Bellinger, D. C. (2012). A strategy for comparing the contributions of environmental chemicals and other risk factors to neurodevelopment of children. *Environmental Health Perspectives*, 120(4), 501–507.

<https://doi.org/10.1289/ehp.1104170>

Chen, L., Liang, S., Liu, M., Yi, Y., Mi, Z., Zhang, Y., et al. (2019). Trans-provincial health impacts of atmospheric mercury emissions in China. *Nature Communications*, 1–12.

<https://doi.org/10.1038/s41467-019-09080-6>

Cheung, W. W. L. (2018). The future of fishes and fisheries in the changing oceans. *Journal of Fish Biology*. <https://doi.org/10.1111/jfb.13558>

Cook, A., Pryer, J., & Shetty, P. (2000). The problem of accuracy in dietary surveys. Analysis of the over 65 UK National Diet and Nutrition Survey. *Journal of Epidemiology and Community Health*.

<https://doi.org/10.1136/jech.54.8.611>

Dutkiewicz, S., Morris, J. J., Follows, M. J., Scott, J., Levitan, O., Dyhrman, S. T., & Berman-frank, I. (2013). Impact of ocean acidification on the structure of phytoplankton communities, 1–19.

<https://doi.org/10.1038/NCLIMATE2722>

Eagles-smith, C. A., Silbergeld, E. K., Basu, N., Bustamante, P., Diaz-barriga, F., Hopkins, W. A., et al. (2018). Modulators of mercury risk to wildlife and humans in the context of rapid global change. *Ambio*, 47(2), 170–197.

<https://doi.org/10.1007/s13280-017-1011-x>

Giang, A., & Selin, N. E. (2016). Benefits of mercury controls for the United States. *Proceedings of the National Academy of Sciences of the United States of America*, 113(2), 286–291.

<https://doi.org/10.1073/pnas.1514395113>

Grandjean, A. C. (2012). Dietary Intake Data Collection: Challenges and limitations. *Nutrition Reviews*.

<https://doi.org/10.1111/j.1753-4887.2012.00545.x>

Grandjean, P., Pichery, C., Bellanger, M., & Budtz-Jorgensen, E. (2012). Calculation of Mercury's Effects on Neurodevelopment. *Environmental Health Perspectives*, 120(12), A452. <https://doi.org/10.1186/1476-069X-11-53>

Griffiths, C., McGartland, A., & Miller, M. (2007). A comparison of the monetized impact of IQ decrements from mercury emissions. *Environmental Health Perspectives*. <https://doi.org/10.1289/ehp.9797>

Halwart, M., & Gupta, M. V. (2004). *Culture of Fish in Rice Fields*. FAO and The WorldFish Center.

Horowitz, H. M., Jacob, D. J., Zhang, Y., Dibble, T. S., Slemr, F., Amos, H. M., et al. (2017). A new mechanism for atmospheric mercury redox chemistry: Implications for the global mercury budget.

Atmospheric Chemistry and Physics, 17(10), 6353–6371. <https://doi.org/10.5194/acp-17-6353-2017>

Karagas, M. R., Choi, A. L., Oken, E., Horvat, M., Schoeny, R., Kamai, E., et al. (2012). Evidence on the human health effects of low-level methylmercury exposure. *Environmental Health Perspectives*.

<https://doi.org/10.1289/ehp.1104494>

- Kocman, D., Wilson, S. J., Amos, H. M., Telmer, K. H., Steenhuisen, F., Sunderland, E. M., et al. (2017). Toward an assessment of the global inventory of present-day mercury releases to freshwater environments. *International Journal of Environmental Research and Public Health*, *14*(2). <https://doi.org/10.3390/ijerph14020138>
- Kwon, S. Y., Selin, N. E., Giang, A., Karplus, V. J., & Zhang, D. (2018). Present and Future Mercury Concentrations in Chinese Rice: Insights From Modeling. *Global Biogeochemical Cycles*, *32*(3), 437–462. <https://doi.org/10.1002/2017GB005824>
- Mozaffarian, D., & Rimm, E. B. (2006). Fish intake, contaminants, and human health evaluating the risks and the benefits. *Journal of the American Medical Association*. <https://doi.org/10.1001/jama.296.15.1885>
- Pacyna, J. M., Travnikov, O., Simone, F. De, Hedgecock, I. M., Sundseth, K., Pacyna, E. G., et al. (2016). Current and future levels of mercury atmospheric pollution on a global scale. *Atmospheric Chemistry and Physics*, *16*(19), 12495–12511. <https://doi.org/10.5194/acp-16-12495-2016>
- Rice, G. E., & Hammitt, J. K. Economic valuation of human health benefits of controlling mercury emissions from U. S. coal-fired power plants (2005). Boston, MA, USA.
- Rice, G. E., Hammitt, J. K., & Evans, J. S. (2010). A probabilistic characterization of the health benefits of reducing methyl mercury intake in the United States. *Environmental Science and Technology*, *44*(13), 5216–5224. <https://doi.org/10.1021/es903359u>
- Rind, D., Lerner, J., Jonas, J., & McLinden, C. (2007). Effects of resolution and model physics on tracer transports in the NASA Goddard Institute for Space Studies general circulation models. *Journal of Geophysical Research Atmospheres*. <https://doi.org/10.1029/2006JD007476>
- Roman, H. A., Walsh, T. L., Coull, B. A., Dewailly, É., Guallar, E., Hattis, D., et al. (2011). Evaluation of the cardiovascular effects of methylmercury exposures: Current evidence supports development of a dose-response function for regulatory benefits analysis. *Environmental Health Perspectives*, *119*(5), 607–614. <https://doi.org/10.1289/ehp.1003012>
- Rothenberg, S. E., & Feng, X. (2012). Mercury cycling in a flooded rice paddy. *Journal of Geophysical Research: Biogeosciences*, *117*(3), 1–16. <https://doi.org/10.1029/2011JG001800>
- Rothenberg, S. E., Windham-myers, L., & Creswell, J. E. (2014). Rice methylmercury exposure and mitigation: A comprehensive review. *Environmental Research*, *133*, 407–423. <https://doi.org/10.1016/j.envres.2014.03.001>
- Salonen, J. T., Seppänen, K., Nyyssönen, K., Korpela, H., Kauhanen, J., Kantola, M., et al. (1995). Intake of mercury from fish, lipid peroxidation, and the risk of myocardial infarction and coronary, cardiovascular, and any death in Eastern Finnish men. *Circulation*. <https://doi.org/10.1161/01.CIR.91.3.645>

- Schartup, A. T., Qureshi, A., Dassuncao, C., Thackray, C. P., Harding, G., & Sunderland, E. M. (2018). A Model for Methylmercury Uptake and Trophic Transfer by Marine Plankton. <https://doi.org/10.1021/acs.est.7b03821>
- Schartup, A. T., Colin, P., Qureshi, A., Dassuncao, C., Gillespie, K., Hanke, A., & Sunderland, E. M. (2019). Climate change and overfishing increase neurotoxicant in marine predators. *Nature*, *572*, 648–650. <https://doi.org/10.1038/s41586-019-1468-9>
- Schmidt, J. A., Wang, S., Jacob, D. J., Horowitz, H. M., Hu, L., Sherwen, T., et al. (2016). Modeling the observed tropospheric BrO background: Importance of multiphase chemistry and implications for ozone, OH, and mercury. *Journal of Geophysical Research*, 1–17. <https://doi.org/10.1002/2015JD024229>
- Schuster, P. F., Schaefer, K. M., Aiken, G. R., Antweiler, R. C., Dewild, J. F., Gryziec, J. D., et al. (2018). Permafrost Stores a Globally Significant Amount of Mercury. *Geophysical Research Letters*, *45*, 1463–1471. <https://doi.org/10.1002/2017GL075571>
- Selin, N. E. (2018). A proposed global metric to aid mercury pollution policy. *Science*, *360*(6389), 607–609. <https://doi.org/10.1126/science.aar8256>
- Selin, N. E., Jacob, D. J., Yantosca, R. M., Strode, S., & Jaegle, L. (2008). Global 3-D land-ocean-atmosphere model for mercury: Present-day versus preindustrial cycles and anthropogenic enrichment factors for deposition, *22*(li), 1–13. <https://doi.org/10.1029/2007GB003040>
- Smith-Downey, N. V., Sunderland, E. M., & Jacob, D. J. (2010). Anthropogenic impacts on global storage and emissions of mercury from terrestrial soils: Insights from a new global model. *Journal of Geophysical Research: Biogeosciences*, *115*(3), 1–11. <https://doi.org/10.1029/2009JG001124>
- Sokolov, A. P., Stone, P. H., Forest, C. E., Prinn, R., Sarofim, M. C., Webster, M., et al. (2009). Probabilistic forecast for twenty-first-century climate based on uncertainties in emissions (without policy) and climate parameters. *Journal of Climate*. <https://doi.org/10.1175/2009JCLI2863.1>
- Spadaro, J. V., & Rabl, A. (2008). Global health impacts and costs due to mercury emissions. *Risk Analysis*, *28*(3), 603–613. <https://doi.org/10.1111/j.1539-6924.2008.01041.x>
- Streets, D. G., Zhang, Q., & Wu, Y. (2009). Projections of Global Mercury Emissions in 2050. *Environmental Science and Technology*, *43*, 2983–2988. <https://doi.org/10.1021/es802474j>
- Trasande, L., Landrigan, P. J., & Schechter, C. (2005). Public health and economic consequences of methyl mercury toxicity to the developing brain. *Environmental Health Perspectives*. <https://doi.org/10.1289/ehp.7743>
- Undeman, E., Brown, T. N., Mclachlan, M. S., & Wania, F. (2018). Who in the world is most exposed to polychlorinated biphenyls? Using models to identify highly exposed populations OPEN ACCESS Who in

the world is most exposed to polychlorinated biphenyls? Using models to identify highly exposed populations.

UNEP. (2017). The Minamata Convention on Mercury.

Wang, F., Outridge, P. M., Feng, X., Meng, B., Heimbürger-Boavida, L. E., & Mason, R. P. (2019). How closely do mercury trends in fish and other aquatic wildlife track those in the atmosphere? – Implications for evaluating the effectiveness of the Minamata Convention. *Science of the Total Environment*.
<https://doi.org/10.1016/j.scitotenv.2019.04.101>

Watson, R. A. (2017). Data Descriptor: A database of global marine commercial , small-scale , illegal and unreported fisheries catch 1950 – 2014, 1–9.

Xue, J., Zartarian, V., Mintz, B., Weber, M., Bailey, K., & Geller, A. (2015). Modeling tribal exposures to methyl mercury from fish consumption. *Science of the Total Environment*.
<https://doi.org/10.1016/j.scitotenv.2015.06.070>

Zhang, H, Holmes, C. D., & Wu, S. (2016). Impacts of changes in climate , land use and land cover on atmospheric mercury, *141*, 230–244. <https://doi.org/10.1016/j.atmosenv.2016.06.056>

Zhang, Hua, Feng, X., Larssen, T., Qiu, G., & Vogt, R. D. (2010). In inland China, rice, rather than fish, is the major pathway for methylmercury exposure. *Environmental Health Perspectives*, *118*(9), 1183–1188.
<https://doi.org/10.1289/ehp.1001915>

Zhang, Y., Jacob, D. J., Horowitz, H. M., Chen, L., Amos, H. M., Krabbenhoft, D. P., et al. (2016). Observed decrease in atmospheric mercury explained by global decline in anthropogenic emissions. *Proceedings of the National Academy of Sciences of the United States of America*, *113*(3), 526–531.
<https://doi.org/10.1073/pnas.1516312113>

Zhang, Y., Horowitz, H., Wang, J., Xie, Z., Kuss, J., & Soerensen, A. L. (2019). A Coupled Global Atmosphere-Ocean Model for Air-Sea Exchange of Mercury: Insights into Wet Deposition and Atmospheric Redox Chemistry. *Environmental Science and Technology*, *53*(9), 5052–5061. research-article. <https://doi.org/10.1021/acs.est.8b06205>

Zhang, Y., Soerensen, A. L., Schartup, A. T., & Sunderland, E. M. (2020). A global model for methylmercury formation and uptake at the base of marine food webs. *Global Biogeochemical Cycles*, *34*, 1–44.
<https://doi.org/10.1029/2019GB006348>

Figures

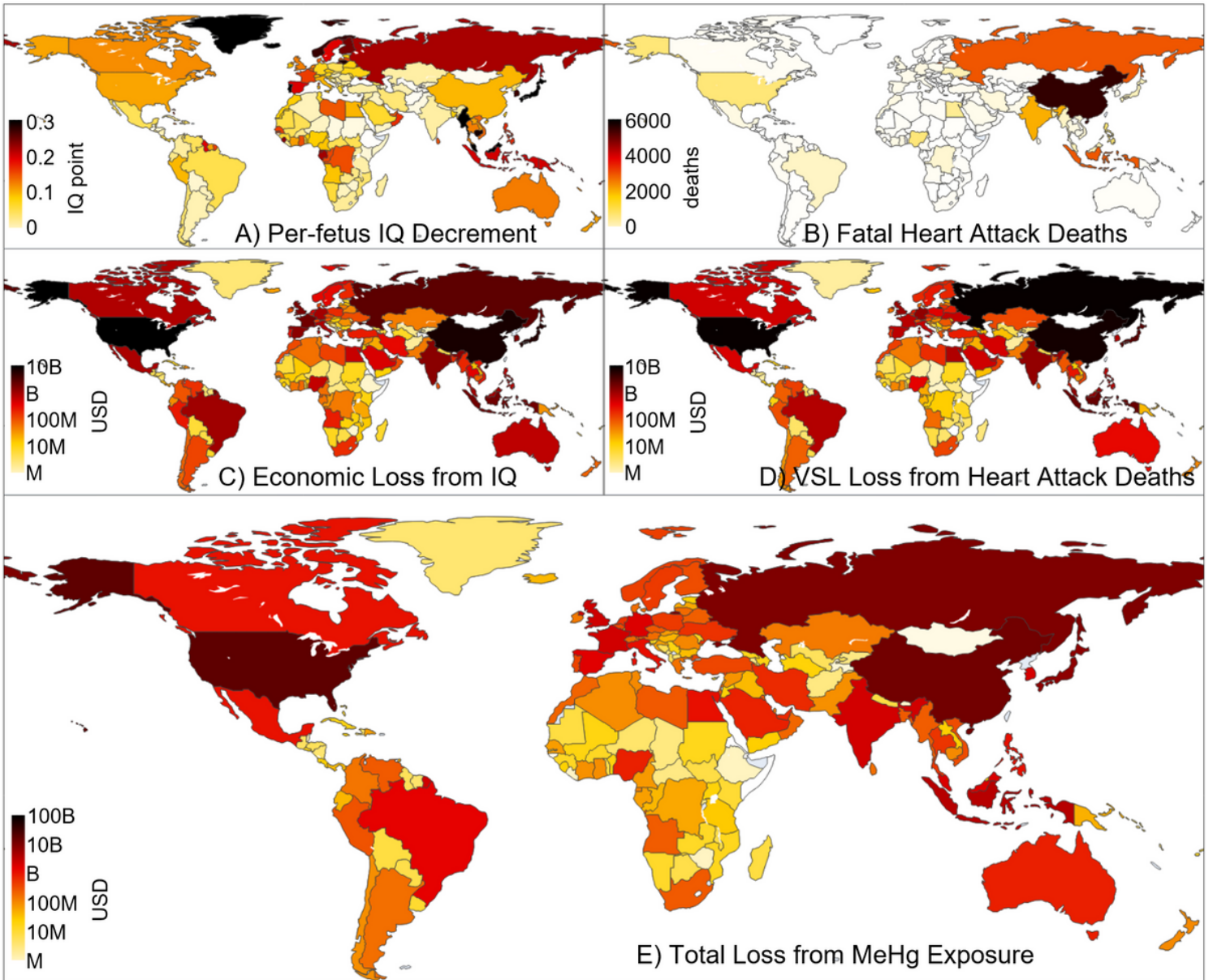


Figure 1

Global health impact of MeHg food exposure at present-day. A) Per-fetus IQ decrement; B) Fatal heart attack deaths; C) Economic loss from IQ decrease; D) Value of statistical life (VSL) loss from fatal heart attacks; E) Total loss from MeHg exposure (the sum of C and D). Economic losses are in US dollars (2020 value and PPP adjusted). The grey area indicates missing data and the color scale of C-E is in the logarithmic scale.

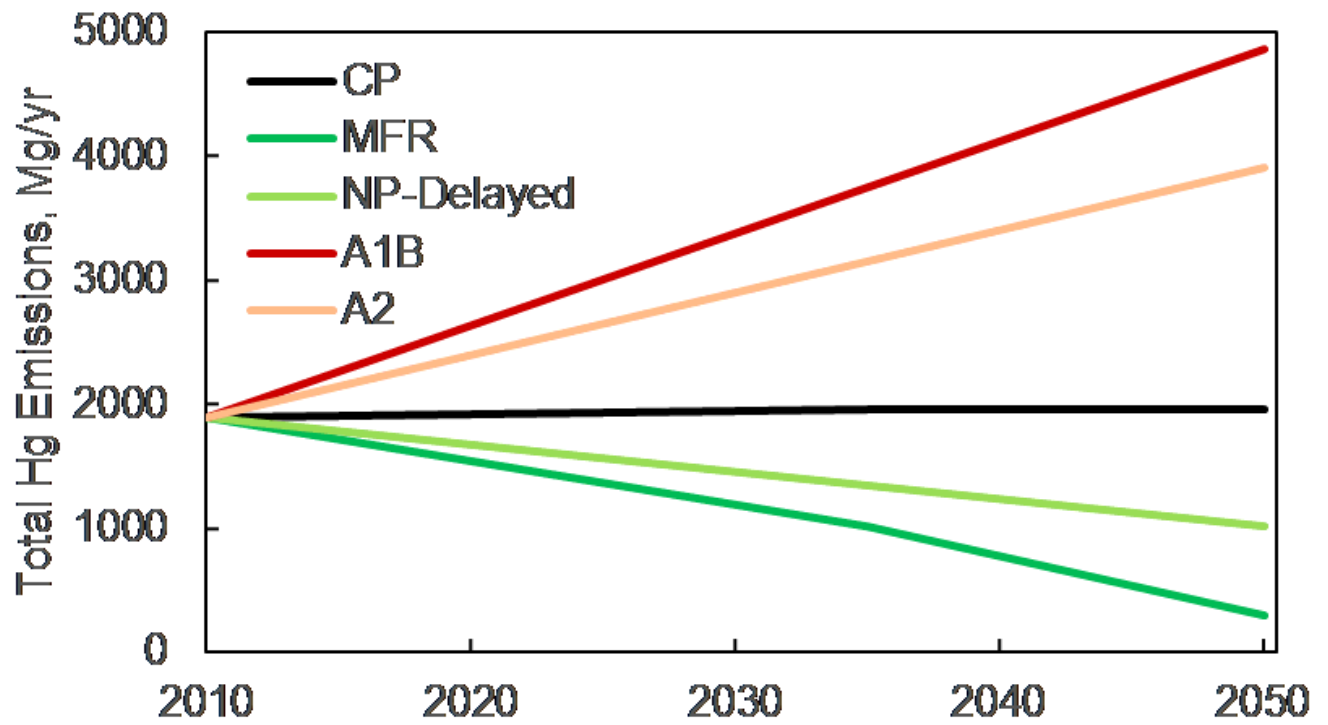


Figure 2

Projections of global total anthropogenic emission of Hg during 2010-2050 based on different emission scenarios (Pacyna et al., 2016; Streets et al., 2009). CP (current policy) scenario assumes a near to constant emissions through 2050. A1B and A2 are for “business as usual” and “a divided world” scenarios with increasing emissions, respectively. MFR (maximum feasible reduction) assumes the application of the best available technologies and aggressive emission reductions. NP-Delayed assumes the 2035 goal of the MFR scenario is delayed to 2050.

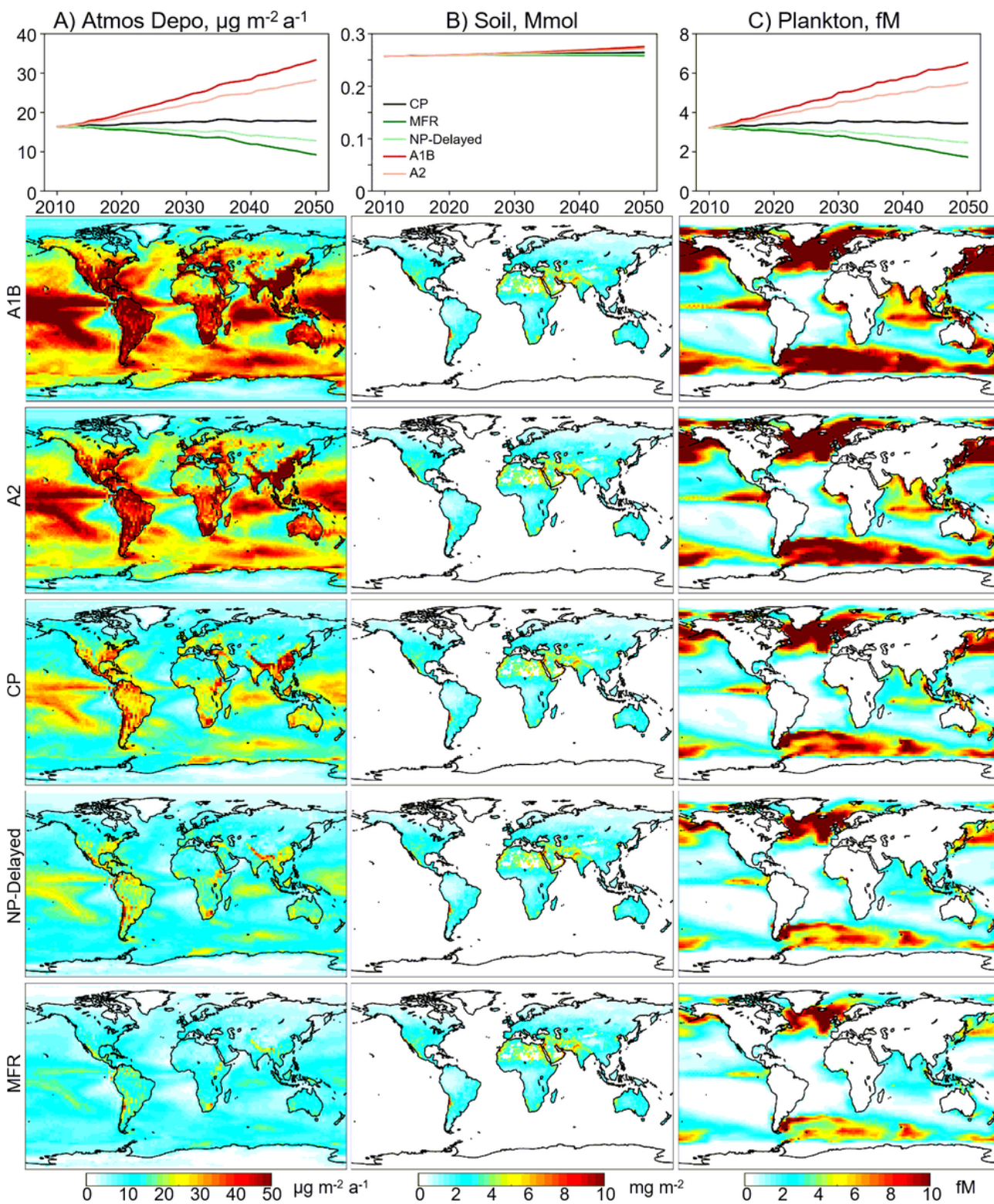


Figure 3

Projected Hg levels in atmospheric deposition (column A), soil (column B), and marine plankton (column C) in 2050. For each column, the top panel shows the trend of global mean values, while the lower panels are the spatial distributions for the five scenarios (with emission from highest to lowest): A1B, A2, CP, NP-Delayed, and MFR.

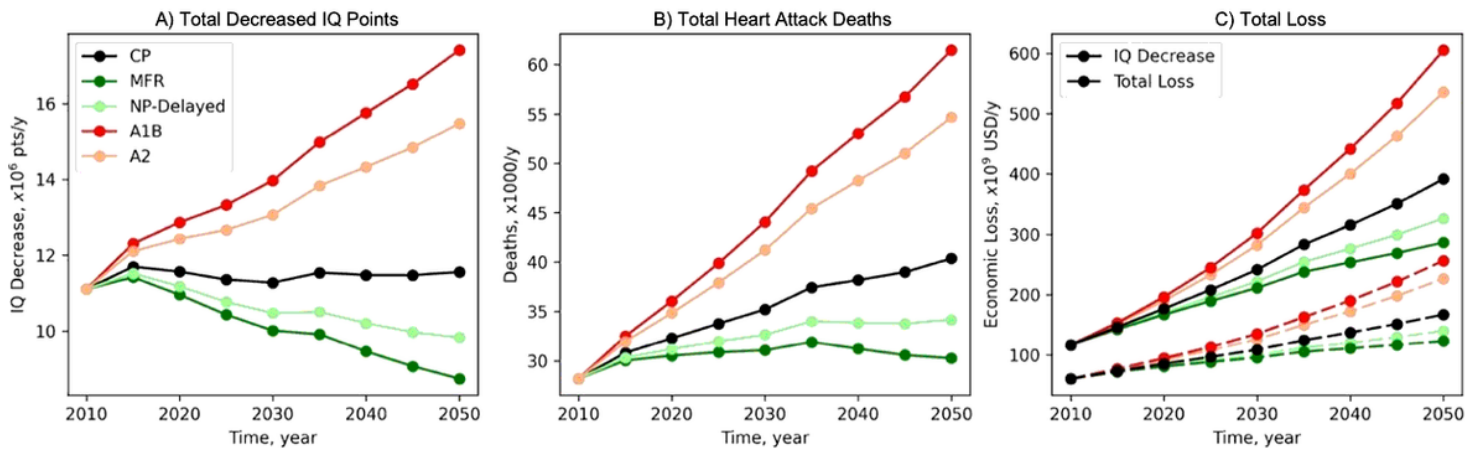


Figure 4

Trajectories of global annual health effects associated with different future emission scenarios. A) Total IQ decrements of newborns; B) Total heart attack deaths; C) Economic valuation of health effects: total valuation (solid lines) and from IQ decrements (dashed lines).

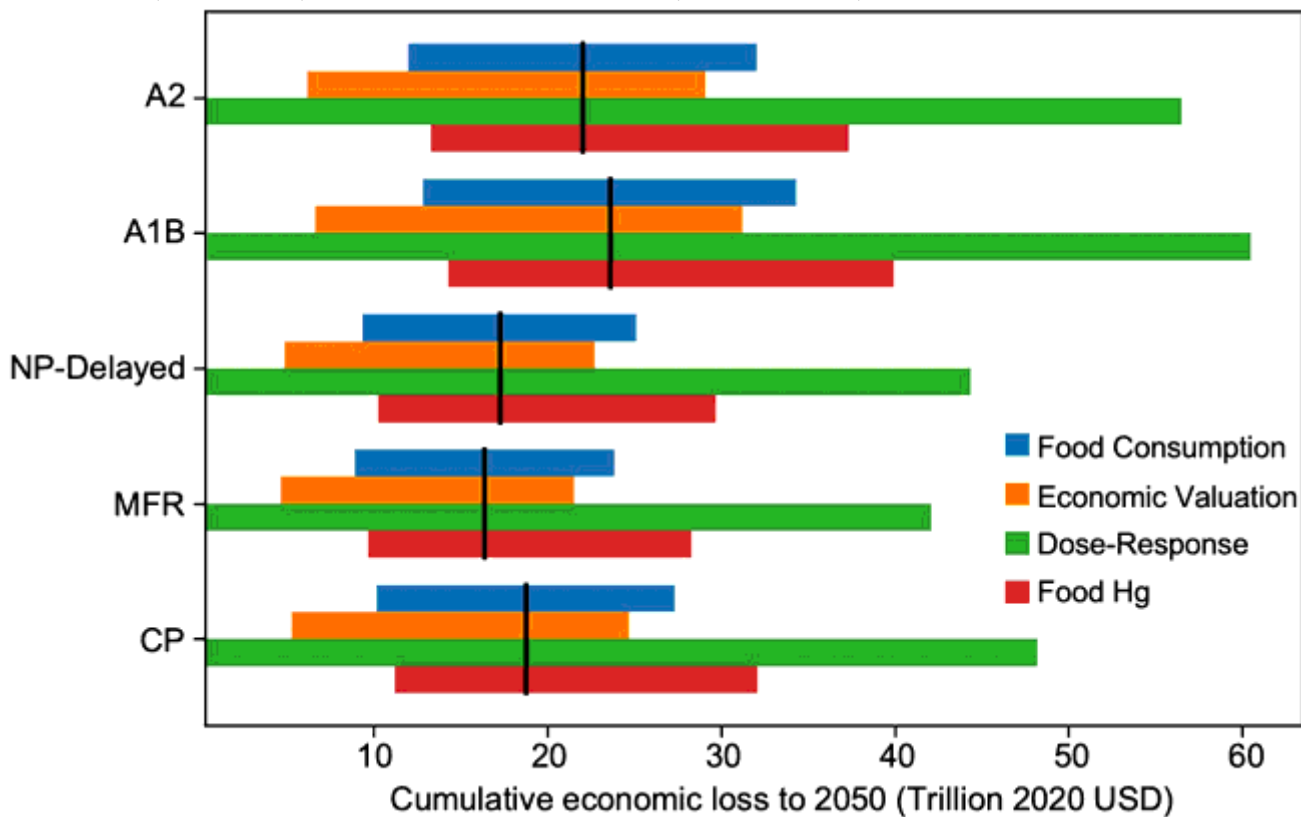


Figure 5

Range in cumulative health impacts to 2050 for the CP, MFR, NP-Delayed, A1B, and A2 scenarios.

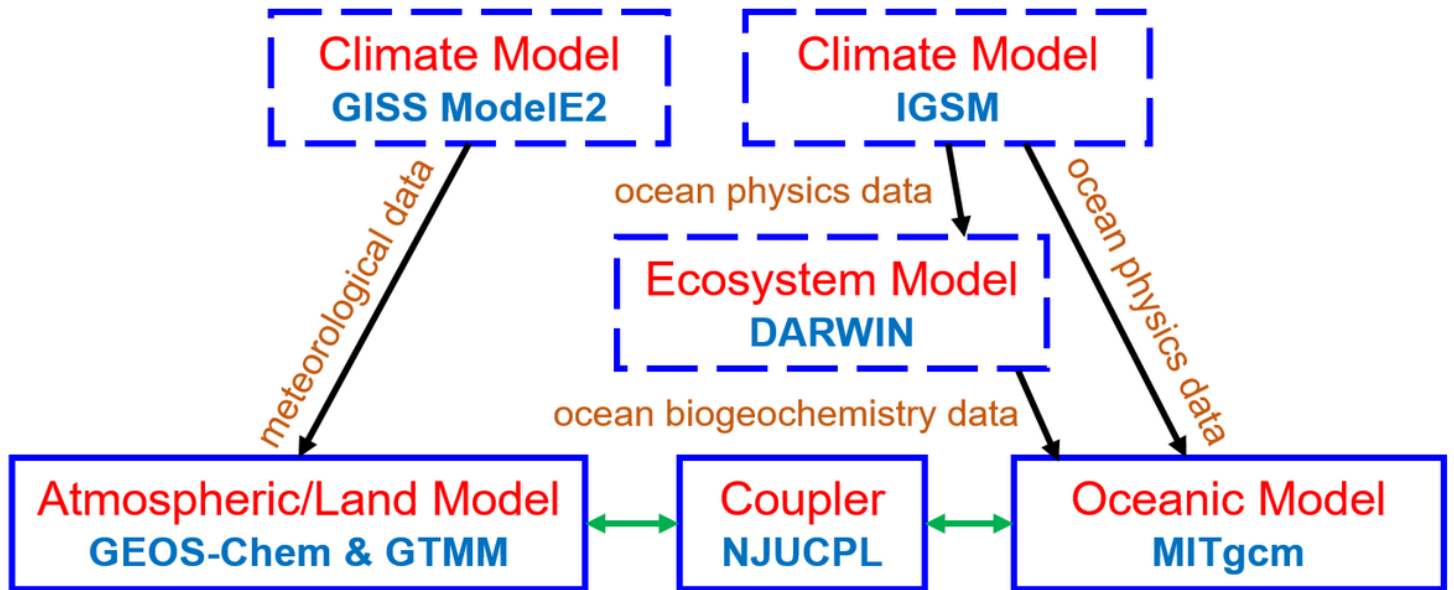


Figure 6

The model framework used in this study. Blue boxes represent models while arrows indicate data flows. Models with dashed boxes are run by previous studies and we directly use their archived output, while those with solid lines are run in this study. Black arrows mean feeding of archived data from one model to another (i.e. models are run separately), while green arrows mean running two models simultaneously with online data exchange.

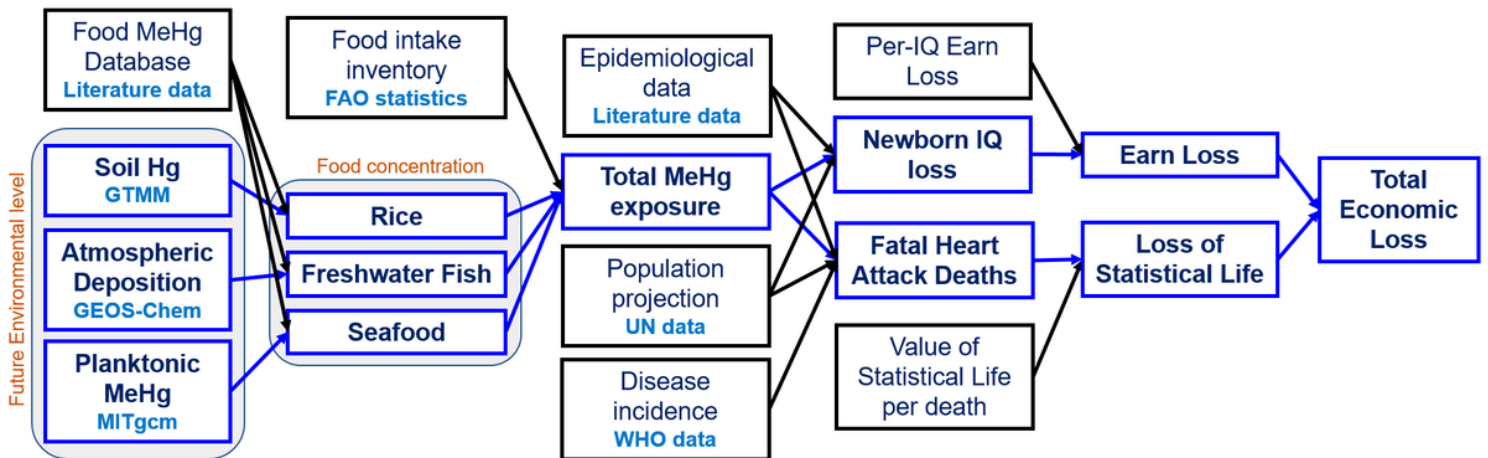


Figure 7

Diagram for the approach and data sources for MeHg exposure and risk calculation in this study. Blue frames represent model calculated variables, while black ones are for literature data.

Supplementary Files

This is a list of supplementary files associated with this preprint. Click to download.

- Slv7.docx
- riskbaseline.xlsx
- rs.pdf